

Laser-Induced Graphene Electrodes for Flexible pH Sensors

Original

Laser-Induced Graphene Electrodes for Flexible pH Sensors / Massaglia, Giulia; Spisni, Giacomo; Serra, Tommaso; Quaglio, Marzia. - In: NANOMATERIALS. - ISSN 2079-4991. - 14:24(2024). [10.3390/nano14242008]

Availability:

This version is available at: 11583/2996411 since: 2025-01-09T09:53:52Z

Publisher:

Multidisciplinary Digital Publishing Institute (MDPI)

Published

DOI:10.3390/nano14242008

Terms of use:

This article is made available under terms and conditions as specified in the corresponding bibliographic description in the repository

Publisher copyright

(Article begins on next page)

RESEARCH ARTICLE | SEPTEMBER 26 2019

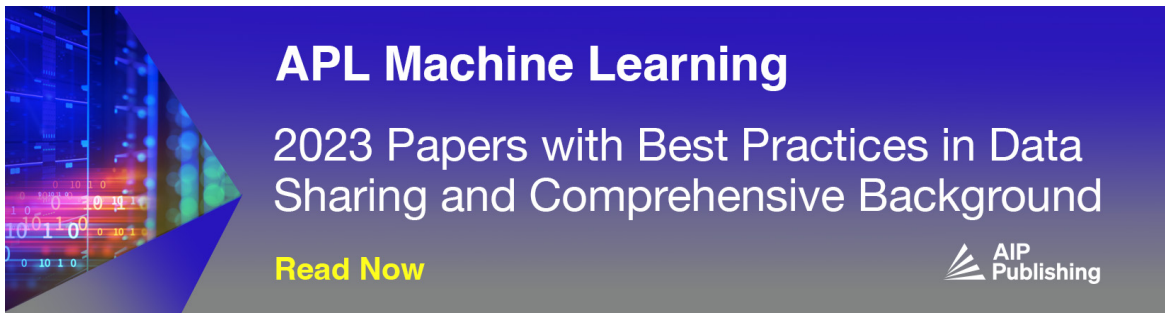
Behavioral modeling of integrated phase-change photonic devices for neuromorphic computing applications

Special Collection: [Emerging Materials in Neuromorphic Computing](#)


Santiago G.-C. Carrillo ; Emanuele Gemo ; Xuan Li; Nathan Youngblood ; Andrew Katumba; Peter Bienstman; Wolfram Pernice; Harish Bhaskaran; C. David Wright  

 Check for updates

APL Mater. 7, 091113 (2019)
<https://doi.org/10.1063/1.5111840>

A promotional banner for "APL Machine Learning". It features a blue background with a graphic of binary code (0s and 1s) and glowing nodes on the left. The text on the right reads: "APL Machine Learning", "2023 Papers with Best Practices in Data Sharing and Comprehensive Background", and "Read Now" in yellow. The AIP Publishing logo is in the bottom right corner.

APL Machine Learning
2023 Papers with Best Practices in Data Sharing and Comprehensive Background
[Read Now](#)



Behavioral modeling of integrated phase-change photonic devices for neuromorphic computing applications

Cite as: APL Mater. 7, 091113 (2019); doi: 10.1063/1.5111840
Submitted: 30 May 2019 • Accepted: 5 September 2019 •
Published Online: 26 September 2019



Santiago G.-C. Carrillo,¹ Emanuele Gemo,¹ Xuan Li,² Nathan Youngblood,² Andrew Katumba,³ Peter Bienstman,³ Wolfram Pernice,⁴ Harish Bhaskaran,² and C. David Wright^{1,a)}

AFFILIATIONS

¹Department of Engineering, University of Exeter, Exeter, United Kingdom

²Department of Materials, University of Oxford, Oxford, United Kingdom

³Ghent University - imec, Ghent, Belgium

⁴Institute of Physics, University of Münster, Münster, Germany

Note: This paper is part of the Special Topic on Emerging Materials in Neuromorphic Computing.

a) Author to whom correspondence should be addressed: david.wright@exeter.ac.uk

ABSTRACT

The combination of phase-change materials and integrated photonics has led to the development of new forms of all-optical devices, including photonic memories, arithmetic and logic processors, and synaptic and neuronal mimics. Such devices can be readily fabricated into photonic integrated circuits, so potentially delivering large-scale all-optical arithmetic-logic units and neuromorphic processing chips. To facilitate in the design and optimization of such large-scale systems, and to aid in the understanding of device and system performance, fast yet accurate computer models are needed. Here, we describe the development of a behavioral modeling tool that meets such requirements, being capable of essentially instantaneous modeling of the write, erase, and readout performance of various integrated phase-change photonic devices, including those for synaptic and neuronal mimics.

© 2019 Author(s). All article content, except where otherwise noted, is licensed under a Creative Commons Attribution (CC BY) license (<http://creativecommons.org/licenses/by/4.0/>). <https://doi.org/10.1063/1.5111840>

Integrated phase-change photonic devices have recently been shown capable of a quite remarkable range of functionality, including binary and multilevel nonvolatile memory,^{1–5} non-von Neumann arithmetic computing,^{6,7} and, the focus of this paper, neuromorphic devices and systems.^{8–11} Indeed, recently, a small-scale but “complete” all-optical neuromorphic computing system comprising interconnected phase-change photonic neurons and synapses and capable of supervised and unsupervised learning was experimentally demonstrated.⁹ To aid in the future development of larger-scale systems, and so exploit effectively the potential of integrated phase-change photonic devices in the areas of neuromorphic, arithmetic, and in-memory computing, it is important to have access to reliable and accurate behavioral models that can simulate device performance in reasonable time scales. This is because full, physically realistic modeling of integrated phase-change photonic devices

and systems is not straightforward, requiring simultaneous handling of interlinked optical, thermal, and phase-switching (amorphization and crystallization) processes, including the effects of any temperature, field, and phase-state induced changes in material/device properties. Usually, such physically realistic approaches to modeling are carried out using finite-element (FE) or finite-difference time-domain (FDTD) methods for the solution of optical and thermal processes, along with nucleation and growth,^{12,13} rate-equation,^{14,15} or cellular automata approaches¹⁶ for modeling the phase-transformation process itself. However, such physically realistic modeling is computationally resource heavy and the simulation of even the seemingly simplest of processes, e.g., the write/erase process in a binary memory type device, can take many hours using quite powerful computer workstations. Clearly, simulating the performance of even the most basic phase-change photonic

computing/processing networks/systems, likely to comprise many hundreds if not thousands of interconnected individual devices, is untenable using such “conventional” methods. A simpler approach is obviously needed, one that encapsulates, in an accurate way, the essential operating characteristics of devices, but one that can be run with modest computing power and produce apparently instantaneous results. It is just such a behavioral model that we outline in this paper.

There are two main types of integrated phase-change photonic device: that based on a straight, rib, or strip type waveguide onto which a phase-change cell is deposited [see Fig. 1(a)] and that based on a microring resonator structure, again onto which a phase-change cell is deposited [see Fig. 1(b)]. The waveguides themselves are often fabricated using silicon nitride, Si_3N_4 , on SiO_2 substrates, though the use of the more industry-compatible silicon-on-insulator (SOI) approach (the latter leading to more compact devices and being more inherently CMOS fabrication compatible) is also attractive. Both device types, shown in Fig. 1, can be, and have been, used for binary and multilevel memory,^{1–3} and both are suitable for the implementation of photonic neurons^{9–11} and synapses.^{8–11} A detailed discussion of the operation of these devices for memory and (arithmetic and neuromorphic) processing applications can be found in the literature (e.g., Refs. 1–3, 6–9), and such discussions will therefore not be repeated here. In brief, however, the presence of the phase-change cell on top of the waveguide modifies the optical propagation within the waveguide, and the transmission of light through the waveguide is significantly very different depending on whether the phase-change cell is in its crystalline or amorphous state. For the commonly used phase-change material $\text{Ge}_2\text{Sb}_2\text{Te}_5$ (or GST for short), for example, the crystalline phase is much more absorbing than the amorphous phase, at the wavelengths (~ 1550 nm) typically used in the integrated photonics field. Thus, in the straight waveguide example of Fig. 1(a), the

optical transmission through the waveguide is significantly lower when the phase-change cell is crystalline as compared to when it is amorphous, and this forms the basis of the readout process (i.e., a low power optical pulse is sent down the waveguide, and its amplitude on transmission through the waveguide depends on whether the phase-change cell is crystalline or amorphous). To switch the state of the phase-change cell, tailored higher-power (cf. in the readout process) optical pulses are sent down the waveguide to either amorphize (i.e., *write* to) the cell or to crystallize (i.e., *erase* it). The operation of the microring type device shown in Fig. 1(b) is somewhat more complicated than that of the straight waveguide configuration, since changing the state of the phase-change cell on the microring changes the ring’s resonant properties and so changes the amount of light that couples in/out from/to the coupling waveguide.

As pointed out above, any behavioral model for the operation of integrated phase-change photonic devices needs to account for three inter-related processes occurring in the cell, namely, (i) the propagation of light through the waveguide, (ii) the heating of the phase-change cell, and (iii) the crystallization and amorphization (and melting) of the phase-change cell. These three interlinked processes are represented in our behavioral approach via simplified electromagnetic, heat transfer, and phase-change models.

The electromagnetic model uses the effective refractive index of the cell to calculate the power (or amplitude) and phase of the optical propagation mode in the cell, along with the heat generation resulting from optical absorption in the phase-change cell. Since the photonic phase-change devices can be relatively large, with the phase-change cells often several micrometers in length, and since the distribution of crystallized/amorphized regions is not necessarily homogeneous with the cell, we usually split the simulation space into many smaller subcells. The power, ΔP_i , absorbed in the i th phase-change subcell can thus be described as follows:

$$\Delta P_i = P_{0i} - P_{0i} e^{-2 \cdot k_0 \cdot L_{\text{cell}} \cdot \text{Im}(n_{\text{eff}})_i}, \quad (1)$$

where P_{0i} is the power at the leading edge of the subcell, k_0 is the free space wave-vector, L_{cell} is the length of the subcell, and $\text{Im}(n_{\text{eff}})_i$ represents the imaginary part of the subcell’s effective refractive index. Using this formula, it is possible to calculate the volumetric heat source in each subcell. The optical phase accumulation, $\Delta\phi_i$, of the propagating mode on having traversed a subcell is modeled using the following expression:

$$\Delta\phi_i = k_0 \cdot L_{\text{cell}} \cdot \text{Re}(n_{\text{eff}})_i. \quad (2)$$

Using the previous result, it is possible to express the total change in optical phase ($\Delta\Phi_{\text{cell}}$) as the difference of the accumulated optical phase for the fully crystalline cell (Φ_{cellFC}) and the summation of the individual change in optical phase for each subcell ($\Delta\phi_i$),

$$\Delta\Phi_{\text{cell}} = \Phi_{\text{cellFC}} - \sum_i \Delta\phi_i, \quad (3)$$

where $\text{Re}(n_{\text{eff}})_i$ is the real part of the effective refractive index of the i th subcell. Reflections at the interfaces between subcells are neglected.

For optical modeling of the microring device of Fig. 1(b), it is also necessary to take account of the transmission and coupling

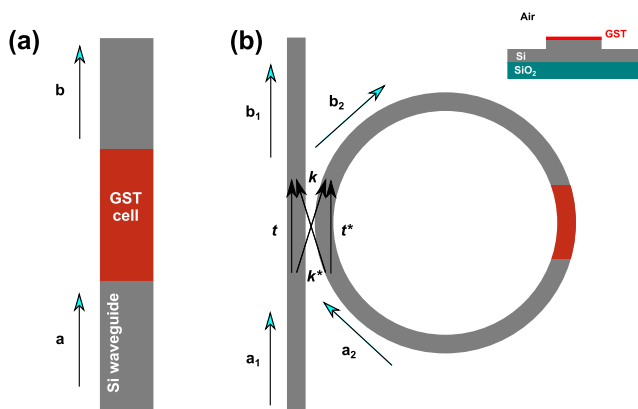


FIG. 1. Integrated phase-change photonic device types. (a) Schematic of the simplest type of device, based on a straight rib type waveguide onto which a micrometer-scale cell of phase-change material is deposited (arrows denote the direction of propagating optical mode). (b) Schematic of the microring type device, with the input/output coupling waveguide also shown. The various labels in (a) and (b) refer to the various propagating modes and coupling coefficients, as explained in main text. The inset in the top right represents a cross section of the waveguide considered for this work, namely, the rib waveguide fabricated on a silicon-on-insulator platform.

coefficients between the ring and the straight (input-output) waveguide. These are related as follows:¹⁷

$$\begin{pmatrix} b_1 \\ b_2 \end{pmatrix} = \begin{pmatrix} t & k \\ -k^* & t^* \end{pmatrix} \begin{pmatrix} a_1 \\ a_2 \end{pmatrix}, \quad (4)$$

where b_1 is the mode that passes the ring, b_2 is the mode that enters into the ring, a_1 is the input mode (to the straight coupling waveguide), and a_2 is the mode that couples again to the input/output waveguide after circulating in the ring. The relationship between the mode (b_2) entering into the ring and the mode (a_2) that couples from the ring back into the input/output waveguide is given by

$$a_2 = \alpha e^{i\theta} b_2, \quad (5)$$

and this enables the derivation of the following expressions for the modes a_2 and b_1 (for a normalized input power of 1 W):

$$b_1 = \frac{-\alpha + t e^{-i\theta}}{-\alpha t^* + e^{-i\theta}}, \quad (6)$$

$$a_2 = \frac{-\alpha k^*}{-\alpha t^* + e^{-i\theta}}, \quad (7)$$

where α and θ are the attenuation and the accumulated optical phase, respectively, after circulating the ring. The coupling and the transmission coefficients, k and t , respectively, are calculated here using approximate analytical expressions.¹⁸ Equations (4)–(7) contain all the necessary information to calculate the amplitude and optical phase of the modes in the ring and input/output coupling waveguide.

The real and imaginary parts of the effective refractive index, n_{eff} , as used in Eqs. (1) and (2), are accessed by the behavioral model via look-up-tables (LUTs), which, in turn, are obtained by 2D FE eigenmode simulation of the waveguide for various optical powers, temperatures, and phase-state configurations. Such FE simulations essentially provide a library file for a particular device type, whose performance over a vast range of input conditions can subsequently be computed in a fast and efficient manner by the behavioral model. Given the fact that the variation of n_{eff} is reasonably smooth, we here sampled the temperature dependency between 290 K and 1290 K with a resolution of 100 K, the power dependency between 0 W and 0.02 W with a resolution of 0.002 W, and the crystallinity dependency from 0 to 1 with a resolution of 0.2, and finally, the wavelength dependency was sampled between 1530 and 1560 nm with a resolution of 15 nm. This produced 2178 combinations for the LUT, with intermediate values obtained via linear interpolation (note that the results of the behavioral model did not vary in any significant way if we used higher-order interpolations, inferring that the LUT resolution did not introduce inaccuracies due to under-sampling).

Heat transfer is approached in the behavioral model by using an electrical circuit analogy to solve the heat diffusion (Fourier) equation.¹⁹ Here, the temperature is analogous to voltage, heat to charge, and heat flux to electrical current. We assume that the heat flow is predominantly one-dimensional, in the downward direction perpendicular to the plane of the phase-change cell (i.e., downwards through the ITO, GST, and Si waveguide layers, and into the substrate). This is a reasonable assumption bearing in mind that the

ITO and phase-change layers are very thin, compared to their lateral extension, and that their thermal conductivity is much lower than that of the underlying Si waveguide. Some longitudinal heat flow is allowed, however, along the Si waveguide [Fig. 2(a)], reflecting the relatively high thermal conductivity of Si. Thermally, each layer within the device in the vicinity of the phase-change cell is thus modeled as a resistor-capacitor network (RCN), as shown in Fig. 2(b).

The thermal model calculates the temperatures at the top, T_t , bottom, T_b , and middle, T_m , of each layer, with these temperatures being described by the following equations:

$$\frac{1}{4} C \frac{dT_t}{dt} = q_t - \frac{T_t - T_m}{R/2}, \quad (8)$$

$$\frac{1}{2} C \frac{dT_m}{dt} = \frac{T_t - T_m}{R/2} - \frac{T_m - T_b}{R/2}, \quad (9)$$

$$\frac{1}{4} C \frac{dT_b}{dt} = \frac{T_m - T_b}{R/2} - q_b, \quad (10)$$

where C and R refer to the capacitances shown in Fig. 2(b), with $C = \rho c_v l$ and $R = l/k$, where ρ is the density, c_v is the specific heat, and l is the length (thickness) and k is the thermal conductivity of the relevant material layer. The parameters used in the heat transfer model are provided in Table I.

Turning to the modeling of the phase-change process itself, as pointed out in the Introduction, there are several methods commonly used in the literature that could be thought of as “physically realistic,” in so much as they try to model crystallization (and in some cases, amorphization too) based on physical processes (e.g., related to the competition between volume and surface energies during the formation and growth of a crystal phase). However, these models tend not to be sufficiently efficient computationally for behavioral modeling, in particular, when they have

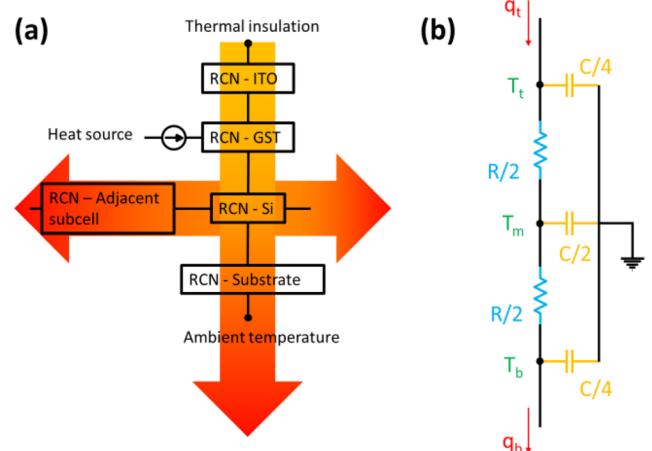


FIG. 2. Thermal model of the photonic phase-change cell. (a) Heat flow in ITO, GST, Si-waveguide, and substrate layers. (b) Resistor-capacitor network (RCN) used to model each layer.

TABLE I. Values of the material density, specific heat, and thermal conductivity used in the heat transfer model.

Material	Density (kg m ⁻³)	Specific heat (J kg ⁻¹ K ⁻¹)	Thermal conductivity (W m ⁻¹ K ⁻¹)
ITO ^a	7120	362.36	5.86
GST	5995 ^b	218 ^b	0.58 ^c
c-Si ^d	2329	700	100
Substrate ^e	2202.7	755.6	73.8

^aReference 25.^bReference 26.^cReference 27.^dFrom COMSOL Multiphysics library (adjusted for layer thickness).^eThe substrate thermal parameters emulate the effect of the heat flowing away from the cell (lateral through c-Si and down to SiO₂) and should be close or lie between the bounds formed by c-Si and SiO₂.

to be interlinked, as in our case, with electromagnetic and thermal simulations. For these reasons, we here use a phenomenological approach based on the well-known Johnson-Mehl-Avrami-Kohnogorov (JMAK) model.^{14,20,21} Here, crystalline fraction χ in the cell is given by the following equation:

$$\chi(t, T) = 1 - \exp\left(-\left(\sum_i K_i \cdot \Delta t\right)^n\right), \quad \text{with} \quad K_i = \nu \exp\left(-\frac{E_a}{k_B T_i}\right), \quad (11)$$

where K_i is the crystallization rate at the i th time iteration, ν is a frequency factor, E_a is the activation energy for crystallization, k_B is the Boltzmann constant, T_i is the temperature in the i th time iteration, n is the Avrami exponent, and Δt is the time increment between iterations in the model. [Note that although the JMAK approach is used mainly in the literature to model only crystallization, the form of Eq. (11) also allows for the simulation of melting and subsequent amorphization, as explained in Ref. 21.] The crystallization behavior predicted by the JMAK approach is controlled by the parameters E_a [slope in the Arrhenius plot of $\ln(t_x)$ vs $1/k_B T$, where t_x is the crystallization time] and ν (intersection as $T \rightarrow \infty$ in the Arrhenius plot), and so it is obviously important to use appropriate values for such parameters. However, it has been widely observed (see, e.g., Refs. 22 and 23) that a single activation energy cannot adequately describe the crystallization behavior of GST; indeed, in the Arrhenius plot, it is clearly possible to observe two regions that can be fitted using different E_a and ν parameters. For example, Ciocchini *et al.*²¹ reported E_a values as small as 0.5 eV in the high-temperature region, but much larger values of around 2 eV at low temperatures. Such a change in E_a also affects the position of the intercept of the Arrhenius plot, i.e., the value of the frequency parameter ν . In this work, therefore, we take E_a as being equal to 1.85 eV for $T < 400^\circ\text{C}$ and 0.5 eV above 400°C . Similarly, ν takes the values 7.35×10^{19} Hz and 8.1×10^9 Hz below and above 400°C , respectively. We set the Avrami coefficient, n , equal to 2.6.¹⁴

Having described the development of the behavioral model above, we now apply it to simulation of the writing, erasing, and reading of data to/from the phase-change cell. The *write* process consists of the amorphization of a previously crystalline cell, while

the *erase* process consists of recrystallization of any amorphous region formed during the write process. *Readout* simply consists of probing, with a suitable low power read pulse, the optical transmission of the device. We begin by considering a straight Si-waveguide device as shown previously in Fig. 1(a) and here with the dimensions as shown in Fig. 3. For simulation purposes, the $4\ \mu\text{m}$ long GST cell is here split into 40 subcells each of 100 nm in length (this resolution was found to be a good compromise between complexity, accuracy, and speed). To write to the GST cell, a relatively high power (here 17 mW) optical pulse of 25 ns duration is sent down the waveguide, as shown in Fig. 4(a) (Multimedia view). The temperature in each of the 40 subcells that make up the GST cell is calculated at each time step (here taken to be 1 ns), along with the resulting fraction of crystallized material in each subcell [see Figs. 4(b) and 4(c) (Multimedia view), respectively]. Finally, the optical transmission, T_r , through the waveguide (equivalent to the readout signal) is calculated, as shown in Fig. 4(d) (Multimedia view). Note that the image shown in Fig. 4 (Multimedia view) is the result of the simulation at $t = 45$ ns. A link to an animation showing the results generated in the complete simulation can be found in the caption of Fig. 4 (Multimedia view). In each frame of the simulation, we show the temporal evolution of the applied power and the transmittance in Figs. 4(a) and 4(d) (Multimedia view) and a snapshot of the temperature and phase distributions along the cell in Figs. 4(b) and 4(c) (Multimedia view), respectively. From Fig. 4 (Multimedia view), it can be seen that, as expected, the crystalline fraction is reduced on writing (an amorphous mark is written into the cell, but this does not occupy the whole cell volume), and after thermalization, the optical transmission is increased due to the lower absorption (lower k value) of the amorphous phase.

We now turn our attention to the erase process. Here, we use a double-step pulse, i.e., a pulse with an initially high optical power immediately followed by a longer, lower power segment, which has previously been shown to provide good control of the recrystallization process.^{3,24} This double-step pulse is applied to a cell that has previously been subject to the write cycle shown in Fig. 4 (Multimedia view). Thus, in Fig. 5 (Multimedia view), we show the result of applying a double-step erase pulse comprising 17 mW for 25 ns, followed immediately by 8.5 mW for 700 ns [Fig. 5(a) (Multimedia view)]. Again, we show the temperature and crystal fraction in each subcell [Figs. 5(b) and 5(c) (Multimedia view)], along with the optical transmission through the waveguide [Fig. 5(d) (Multimedia view)]. By the end of the erase pulse, the cell is, as desired, fully recrystallized (run the associated video file to follow the evolution of crystallized fraction throughout the entire erase process).

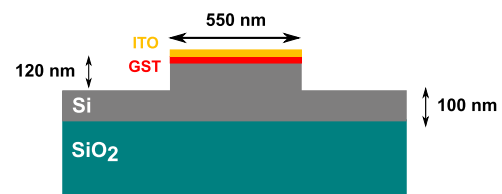


FIG. 3. Detailed layout of a straight rib Si-waveguide phase-change photonic cell. The phase-change layer is a 10 nm thick GST layer protected by a 10 nm thick ITO layer. The length of the phase-change cell is $4\ \mu\text{m}$. The waveguide itself is fabricated in Si and is 550 nm wide and 120 nm high.

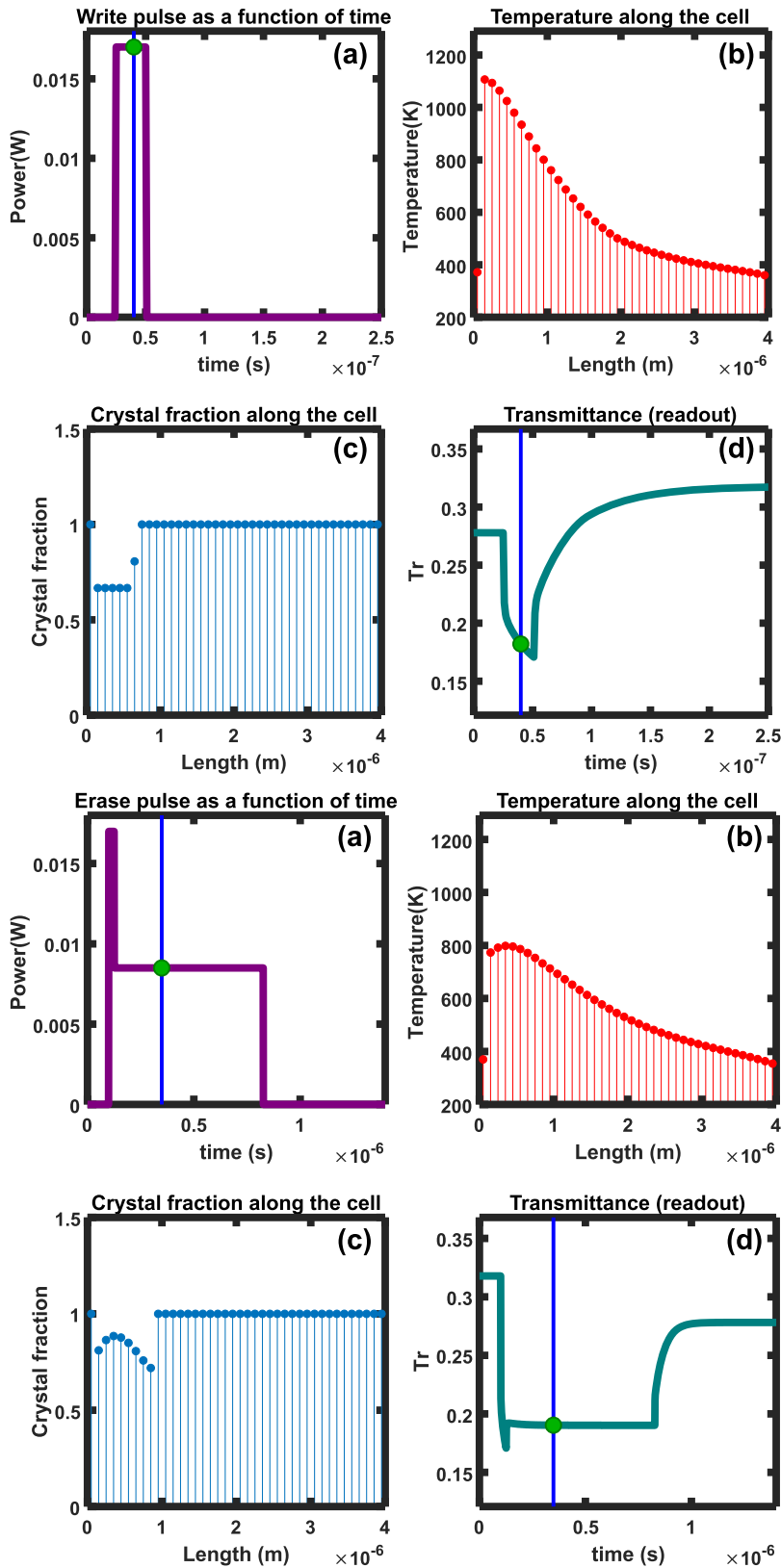


FIG. 4. The writing of an amorphous mark into a previously fully crystalline GST cell in the device configuration of Fig. 3. (a) Form of the write pulse used (here a 25 ns, 17 mW rectangular pulse). (b) Temperature in each of the 40 simulation subcells that make up the $4 \mu\text{m}$ GST cell [at the time indicated by the vertical blue cursor in (a)]. (c) The crystal fraction in each of the subcells [at the time indicated by the vertical blue cursor in (a)]. (d) The change in optical transmission during and after the application of the write pulse. For full simulation results for variation of write pulse power, temperature, crystal fraction, and optical transmission during and after the application of the write (amorphization) pulse, see the accompanying video. Multimedia view: <https://doi.org/10.1063/1.5111840.1>

FIG. 5. The erasing of an amorphous mark [as written as in Fig. 4 (Multimedia view)] using the double-step pulse approach. (a) Form of the erase pulse used (here a double-step pulse with a first segment comprising 17 mW for 25 ns, followed immediately by 8.5 mW for 700 ns). (b) Temperature in each of the 40 simulation subcells that make up the entire $4 \mu\text{m}$ long GST cell [at the time indicated by the vertical blue cursor in (a)]. (c) The crystal fraction in each of the subcells [at the time indicated by the vertical blue cursor in (a)]. (d) The change in optical transmission during and after the application of the erase pulse. For full simulation results for variation of erase pulse power, temperature, crystal fraction, and optical transmission during and after the application of the erase (recrystallization) pulse, see the accompanying video. Multimedia view: <https://doi.org/10.1063/1.5111840.2>

28 June 2024 20:38:11

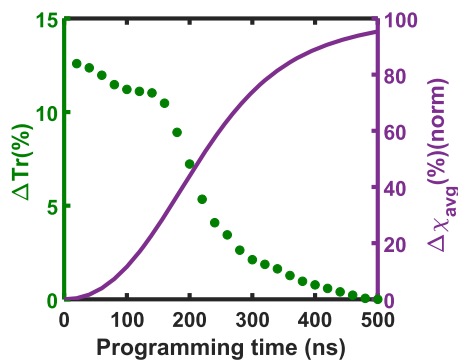


FIG. 6. Storing of multilevel states. Here, the erase pulse of Fig. 5(a) (Multimedia view) is curtailed at different durations ranging from 0 to 600 ns after the application of the first segment of the double-step pulse, resulting in control of the fraction of recrystallization obtained. Left axis shows the change in optical transmission as a function of the length of (the second segment of) the erase pulse. Right axis shows the (normalized) change in fractional crystallization.

Note that by varying the amplitude and/or the duration of the second segment of the double-step pulse of the form shown in Fig. 5(a) (Multimedia view), it is possible to set the phase-change cell into various final crystallization states. This gives access to multilevel capabilities needed for neuromorphic applications (e.g., for the setting of synaptic weights), as shown, for example, in Fig. 6 [also note that multilevel states can also be accessed via the degree of amorphization achieved in the write process, controlled by varying the power and duration of the write pulse of the form shown in Fig. 4(a) (Multimedia view)].

As a final example of the capabilities of the behavioral model, we show in Fig. 7 the simulated readout signal for a device having the microring architecture of Fig. 1(b) and with the phase-change cell crystallized to various fractional levels. For these simulations, the microring is of diameter $19.05 \mu\text{m}$, the gap between the ring and the coupling waveguide is 150 nm, and the rest of the waveguide

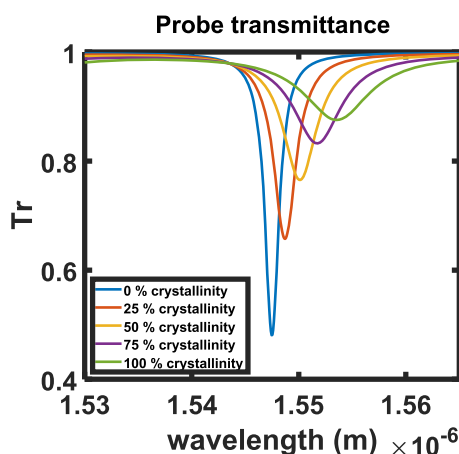


FIG. 7. Readout characteristics of the microring type device architecture. The optical transmission through the coupling waveguide as a function of the fractional crystallization of the phase-change cell located on the microring resonator.

and film dimensions are as given in Fig. 3. It is clear from the results of Fig. 7 that the readout signal (i.e., the optical transmission through the coupling waveguide) changes dramatically with the degree of crystallization. Indeed, as previously observed experimentally,² both the wavelength and the amplitude of the minimum in transmission change as the fraction of crystallized material changes (i.e., as the cell is set to various multilevel states).

Having demonstrated above some of the attributes and capabilities of our behavioral model, we now make a direct comparison of simulated results to experimental data. Thus, we wrote to a fully crystalline cell (on a straight Si waveguide device) with rectangular optical pulses of power 13.23 mW and a range of durations (specifically 10, 20, 50, 75, 100, 125, 150, 175, and 200 ns) while monitoring (using a continuous wave laser of low power) the waveguide's optical transmission. The results are shown in Fig. 8, where a good match between experiment [Fig. 8(a)] and simulation [Fig. 8(b)] can be

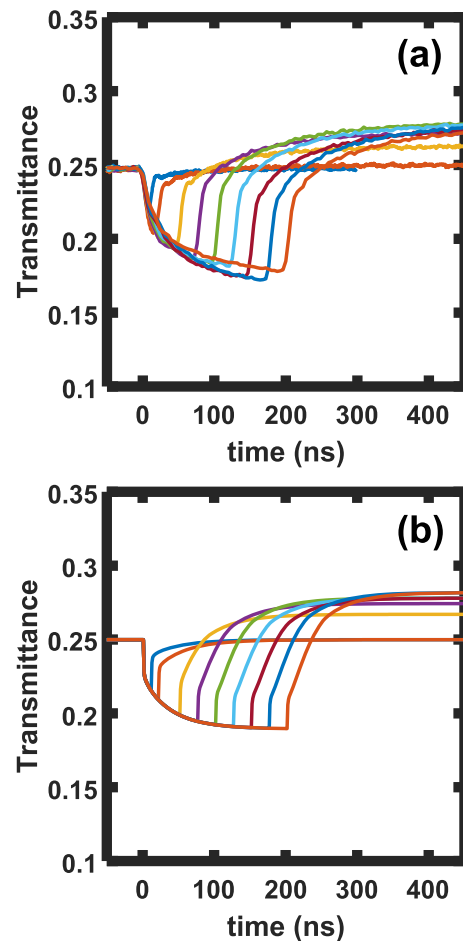


FIG. 8. Comparison of experimental and simulated write performance in the Si-waveguide with the $4 \mu\text{m}$ long phase-change (GST) cell. (a) Variation of experimental waveguide transmission during and after the application of write pulses of durations of 10, 20, 50, 75, 100, 125, 150, 175, and 200 ns (all with power 13.23 mW). (b) Behavioral model simulations for the same device and conditions as in (a).

seen. In both cases (experiment and simulation), the shorter duration pulses do not induce any permanent change in transmission, meaning that little or no amorphization occurred. However, longer duration pulses (specifically 50 ns and above) did result in permanent changes in transmission, indicating successful amorphization. For pulse durations of 75 ns and above, the change in transmission saturated, indicating that, for this optical power and for this particular device, no significant increases in amorphized volume occurred in the cell for pulses longer than 75 ns.

In summary, we have developed a fast, computationally efficient behavioral model for integrated phase-change photonic devices which is capable of simulating their write, erase, and read processes. Thus, the model simulates the performance of such devices when used not only as binary and multilevel memories but also for arithmetic or logic processing and, importantly, as synaptic and neuronal mimics for neuromorphic computing applications. In this work, we have concentrated specifically on the use of the archetypal phase-change material GST, but the model is in no way limited simply to GST and could be used with any phase-change material so long as suitable material parameters were available (specifically, the real and imaginary parts of the refractive index, thermal conductivity and specific heat and density, along with activation energies, etc., used for the JMAK approach). Indeed, since the behavioral model runs in seconds as compared to several hours for equivalent FE models, it could provide a useful tool for the comparison of the likely performance of various phase-change alloys. Furthermore, it should prove extremely useful in the design and simulation of future integrated phase-change photonic systems, including neuromorphic photonic processors.

This work was supported via the European Union's Horizon 2020 Research and Innovation Program (Grant No. 780848, Fun-COMP project) and the UK's Engineering and Physical Sciences Research Council [the EPSRC CDT in Metamaterials (Grant No. EP/L015331/1), the WAFT Collaboration (Grant No. EP/M015173/1), and the Chalcogenide Advanced Manufacturing Partnership (Grant No. EP/M015130/1)]. Data relating to this paper available, on reasonable request, from the corresponding author.

REFERENCES

- ¹C. Rios, P. Hosseini, C. D. Wright, H. Bhaskaran, and W. H. P. Pernice, *Adv. Mater.* **26**, 1372 (2014).
- ²C. Rios, M. Stegmaier, P. Hosseini, D. Wang, T. Scherer, C. D. Wright, H. Bhaskaran, and W. H. P. Pernice, *Nat. Photonics* **9**, 725 (2015).
- ³X. Li, N. Youngblood, C. Rios, Z. Cheng, C. D. Wright, W. H. Pernice, and H. Bhaskaran, *Optica* **6**, 1 (2019).
- ⁴H. Zhang, L. Zhou, B. M. A. Rahman, X. Wu, L. Lu, Y. Xu, J. Xu, J. Song, Z. Hu, L. Xu, and J. Chen, *IEEE Photonics J.* **10**, 1 (2018).
- ⁵J. Zheng, A. Khanolkar, P. Xu, S. Colburn, S. Deshmukh, J. Myers, J. Frantz, E. Pop, J. Hendrickson, J. Doylend, N. Boechler, and A. Majumdar, *Opt. Mater. Express* **8**, 1551 (2018).
- ⁶J. Feldmann, M. Stegmaier, N. Gruhler, C. Rios, H. Bhaskaran, C. D. Wright, and W. H. P. Pernice, *Nat. Commun.* **8**, 1256 (2017).
- ⁷C. Rios, N. Youngblood, Z. Cheng, M. Le Gallo, W. H. P. Pernice, C. D. Wright, A. Sebastian, and H. Bhaskaran, *Sci. Adv.* **5**, eau5759 (2019).
- ⁸Z. Cheng, C. Rios, W. H. P. Pernice, C. D. Wright, and H. Bhaskaran, *Sci. Adv.* **3**, e1700160 (2017).
- ⁹J. Feldmann, N. Youngblood, C. D. Wright, H. Bhaskaran, and W. H. P. Pernice, *Nature* **569**, 208 (2019).
- ¹⁰I. Chakraborty, G. Saha, A. Sengupta, and K. Roy, *Sci. Rep.* **8**, 12980 (2018).
- ¹¹I. Chakraborty, G. Saha, and K. Roy, *Phys. Rev. Appl.* **11**, 014063 (2019).
- ¹²J. A. Kalb, *Crystallization Kinetics in Antimony and Tellurium Alloys Used for Phase Change Recording* (University of Aachen, 2001).
- ¹³A. Sebastian, M. Le Gallo, and D. Krebs, *Nat. Commun.* **5**, 4314 (2014).
- ¹⁴S. Senkader and C. D. Wright, *J. Appl. Phys.* **95**, 504 (2004).
- ¹⁵C. D. Wright, K. Blyuss, and P. Ashwin, *Appl. Phys. Lett.* **90**, 063113 (2007).
- ¹⁶P. Ashwin, B. S. V. Patnaik, and C. D. Wright, *J. Appl. Phys.* **104**, 084901 (2008).
- ¹⁷A. Yariv, *Electron. Lett.* **36**, 321 (2000).
- ¹⁸B. E. Little, S. T. Chu, H. A. Haus, J. Foresi, and J.-P. Laine, *J. Lightwave Technol.* **15**, 998 (1997).
- ¹⁹K.-L. He, Q. Chen, E. Dong, W.-C. Ge, J.-H. Hao, and F. Xu, *Appl. Therm. Eng.* **129**, 1551 (2018).
- ²⁰B. A. William Johnson and R. F. Mehl, in *Metals Technology 1939 Volume VI, Reaction Kinetics in Processes of Nucleation and Growth, August 1939, T. P. No. 1089* (AIME, 1939).
- ²¹C. D. Wright, L. Wang, P. Shah, M. M. Aziz, E. Varesi, R. Bez, M. Moroni, and F. Cazzaniga, *IEEE Trans. Nanotechnol.* **10**, 900 (2011).
- ²²Y. Choi, M. Jung, and Y.-K. Lee, *Electrochem. Solid-State Lett.* **12**, F17 (2009).
- ²³N. Ciochini, M. Cassinerio, D. Fugazza, and D. Ielmini, *IEEE Trans. Electron Devices* **60**, 3767 (2013).
- ²⁴C. Rios, M. Stegmaier, Z. Cheng, N. Youngblood, C. D. Wright, W. H. P. Pernice, and H. Bhaskaran, *Opt. Mater. Express* **8**, 2455 (2018).
- ²⁵T. Ashida *et al.*, *J. Appl. Phys.* **105**, 073709 (2009).
- ²⁶Y. Liu *et al.*, *J. Appl. Phys.* **112**, 123526 (2012).
- ²⁷H.-K. Lyee *et al.*, *Appl. Phys. Lett.* **89**, 151904 (2006).